analytical chemistry

pubs.acs.org/ac Article

Molecular Characterization of Composition and Volatility of Ambient Organic Aerosol Sampled by an UAV-Mounted Portable Aethalometer

Qiaorong Xie, Eli Windwer, Isaac S. Morton, Kelsey E. Lavin, Emily R. Halpern, Dori Nissenbaum, Sergey A. Nizkorodov, Yinon Rudich, and Alexander Laskin*

Cite This: *Anal. Chem.* 2025, 97, 17743−17751 Read Online

ACCESS | Metrics & More | Article Recommendations | Supporting Information

ABSTRACT: Aethalometers are commonly used to measure light absorption by brown carbon (BrC) components of organic aerosols (OA), but they offer limited insight into OA composition. In this study, an unmanned aerial vehicle (UAV) was equipped with a microaethalometer and an optical particle counter (OPC) to measure multiwavelength absorption coefficients and aerosol mass concentrations, while collecting ambient OA samples at 15 and 200 m flight altitudes over an urban area. The collected aethalometer samples were analyzed using an advanced analytical chemistry measurement platform that combines temperature-programmed desorption (TPD) with direct analysis in real-time (DART) ionization and high-resolution mass spectrometry (HRMS), enabling combined optical and molecular characterization. Results show significantly higher OA mass concentrations and light absorption near the surface at 15 m compared to 200 m, reflecting strong local ground-level emissions. Apparent enthalpies of evaporation and saturation vapor mass concentrations of OA components derived from TPD-DART-HRMS measurements agreed well with published values. The particle-phase composition, volatility, and viscosity of OA exhibited comparable characteristics between samples collected at two altitudes with a little variation. This study demonstrates the value of combining UAV-based aethalometer sampling with TPD-DART-HRMS for untargeted molecular analysis of ambient OA. This integrated approach enables simultaneous evaluation of light absorption, volatility, and viscosity—offering a powerful tool for advancing the understanding of BrC chemistry and aerosol processes.

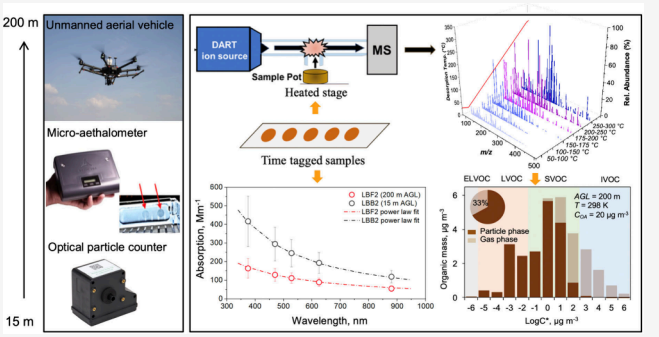

INTRODUCTION

Atmospheric organic aerosol (OA) contains significant amounts of light-absorbing material known as brown carbon (BrC),[1,2] predominantly emitted from the incomplete combustion of biomass and fossil fuels.[3] BrC contributes to climate warming, with its impact partially determined by its atmospheric lifetime.[4,5] A key factor influencing BrC fate is the volatility of its components, which governs their gas-particle partitioning.[6,7] The microaethalometer, which measures filter-based light attenuation by particles collected on a filter, is widely used to assess multiwavelength light absorption by atmospheric particles, and is commonly used to quantify the amount of BrC. Its portability, relatively low cost, and ease of use make it ideal for deployment on mobile platforms, including unmanned aerial vehicles (UAVs).[8,9] In field studies, aethalometer data are often complemented by chemical speciation measurements from colocated instruments such as aerosol mass spectrometers.[10] While primarily used for optical measurements, the microaethalometer also collects samples on PTFE filter tape that can in principle be utilized for molecular analysis. However, detailed chemical analysis of microaethalometer samples has not been attempted before this work because of the challenges associated with the small sample size and low mass loadings, typically confined to a ∼3 mm spot on the PTFE filter tape.

Recent advancements have significantly improved the ability to characterize OA composition and volatility. A novel experimental approach combines thermal evaporation of small OA samples using a temperature-programmed desorption (TPD) stage interfaced with the direct analysis in real time (DART) ionization source and high-resolution mass spectrometer (HRMS).[11] This setup allows for direct analysis of substrate-deposited OA samples without additional sample preparation.[11] Notably, the method enables direct measurement of apparent enthalpies of the condensed-phase to gas-phase

Received: May 20, 2025
Revised: July 8, 2025
Accepted: July 28, 2025
Published: August 6, 2025

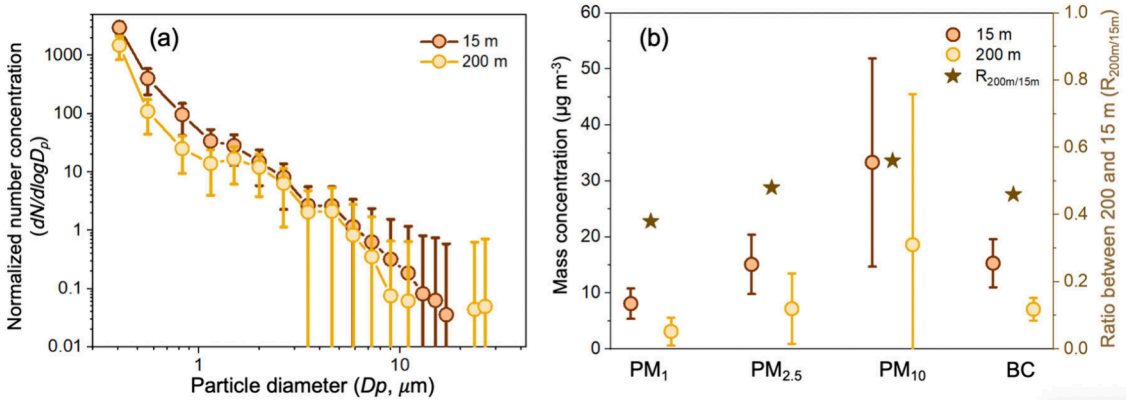

Figure 1. (a) OPC measured particle number size distributions and (b) calculated particle mass concentrations at 15 and 200 m altitude. The brown stars present the ratio of particle mass concentrations measured at 200 and 15 m altitudes.

transition ($^{i}\Delta H^{*}$, kJ mol^{-1}) and saturation vapor pressures ($^{i}p_{T}^{*}$, Pa) of individual species (i).[12] These parameters enable the construction of volatility basis set (VBS) distributions, which quantify gas−particle partitioning, and also allow for estimation of OA viscosity. This, in turn, informs diffusion rates, mixing times, and the extent of multiphase chemical processing, critical for predicting OA behavior and atmospheric evolution.[13−15]

In this study, a hexacopter UAV drone was equipped with a hand-held microaethalometer to measure multiwavelength light absorption and collect the ambient aerosol samples at 15 and 200 m flight altitudes during the Lag Ba'Omer 2023 national festival in Israel. This event was characterized by intense biomass burning OA (BBOA) emissions from widespread festival bonfires. The collected samples were analyzed using TPD-DART-HRMS to determine the chemical composition and quantify the apparent enthalpies $^{i}\Delta H^{*}$ (kJ mol^{-1}) and gas-phase effective saturation mass concentrations $^{i}C_{T}^{*}$ of individual OA components. These data enabled the construction of VBS distributions to quantitatively assess gas-particle partitioning and viscosity of OA mixtures under atmospherically relevant conditions. This work demonstrates the deployment of a hand-held microaethalometer on a UAV drone for simultaneous measurements of optical properties and molecular characterization of OA composition and volatility, offering a novel and valuable approach for advancing aerosol chemistry research, particularly in the context of BBOA.

EXPERIMENTAL AND ANALYSIS METHODS

Field Deployment and Real-Time Measurements. A Matrice 600 Pro hexacopter drone (SZ DJI Technology Co., Shenzhen, China) was outfitted with a microaethalometer (MA200; AethLabs, California, USA) and an optical particle counter (OPC-N3, Alphasense, Essex, UK) (Figure S1). The MA200 is a filter-based optical photometer that measures light attenuation caused by particle accumulation on a 3 mm diameter sampling area (hereafter referred to as the "spot") on an automatically advancing PTFE filter tape. It uses five light-emitting diodes (LEDs) of 375, 470, 528, 625, and 880 nm to intermittently illuminate the spot, and photomultiplier detectors measure transmitted light through the particle-laden filter. A microprocessor calculates changes in light attenuation to derive black carbon (BC) and BrC mass concentrations.[16] The MA200 operated in "DualSpot" mode for real-time correction, with a $PM_{2.5}$ cyclone inlet, 0.1 L min^{-1} flow rate, and 5-s data intervals for optimal signal-to-noise ratio. A 30 min equilibration preceded each flight. The OPC-N3 was deployed alongside the MA200 to measure particle number size distributions (PNSD) and estimate PM mass concentrations.[17] Its utility in UAV-based missions has been demonstrated in previous studies.[18] Further details on the UAV field operation, real-time measurements from the MA200 and OPC-N3, and associated data analysis are provided in Supplemental Note 1.

UAV flights were conducted on May 8, 2023, during the Lag Ba'Omer festival at the campus of the Weizmann Institute of Science (WIS), Rehovot, Israel - a night marked by widespread bonfire activity. Two 20 min stationary flights were performed at 15 and 200 m above ground level (AGL) (Figures S1−S3). The UAV was piloted to the assigned height and kept stationary for the duration of the sampling at that height. The 15-m flight allowed near-surface sampling, while minimizing contributions of coarse dust from the ground and avoiding airmass obstruction by low-rise campus buildings. The event provides a unique opportunity to study biomass burning affected OA in an urban setting.[19−21] There were at least 10 bonfires in the vicinity of the sampling location within a 1 km radius. Meteorological conditions were measured at a weather station located 800 m away: 23.7 ± 3.3 °C, 69% ± 14% RH, and wind speed of 2.2 ± 1.3 m s^{-1} from a southwesterly direction of 204° ± 22°.

Molecular Characterization Experiments and Data Analysis. The aethalometer tape cartridges containing ambient aerosol samples were wrapped in aluminum foil and paraffin film, sealed in Ziploc bags with desiccant packets, and hand-carried to Purdue University (PU) for analysis. Prior to analysis, the samples were stored at −20 °C, except during transport from WIS to PU, which was completed in approximately 24 h. The samples were analyzed using a TPD-DART-HRMS setup, as described in our previous work.[12,14] Briefly, sections of filter tape with the aerosol samples were cut out and mounted onto a copper stub and subjected to a controlled heating TPD profile: starting at 298 K (held for 0.4 min), ramped at 70 K min^{-1} to 623 K, and held for 2 min, yielding a total runtime of 7 min. During the thermal ramp, degassed species were ionized by the DART source and analyzed in real time by a Q-Exactive HF-X Orbitrap mass spectrometer, operated in negative ion detection mode. High-resolution mass spectra were continuously recorded, enabling identification of individual components. Molecular formulas were assigned with elemental constraints of $C_{1-40}H_{1-100}O_{1-25}N_{0-1}$ and a ±2.0 ppm mass tolerance.[22]

From the TPD-DART-HRMS data, the saturation vapor pressure $^{i}p_{T}^{*}$ (Pa) and the saturation gas-phase mass concentration $^{i}C_{T}^{*}$ (μg m^{-3}) of each component (i) were

https://doi.org/10.1021/acs.analchem.5c03027
Anal. Chem. 2025, 97, 17743−17751

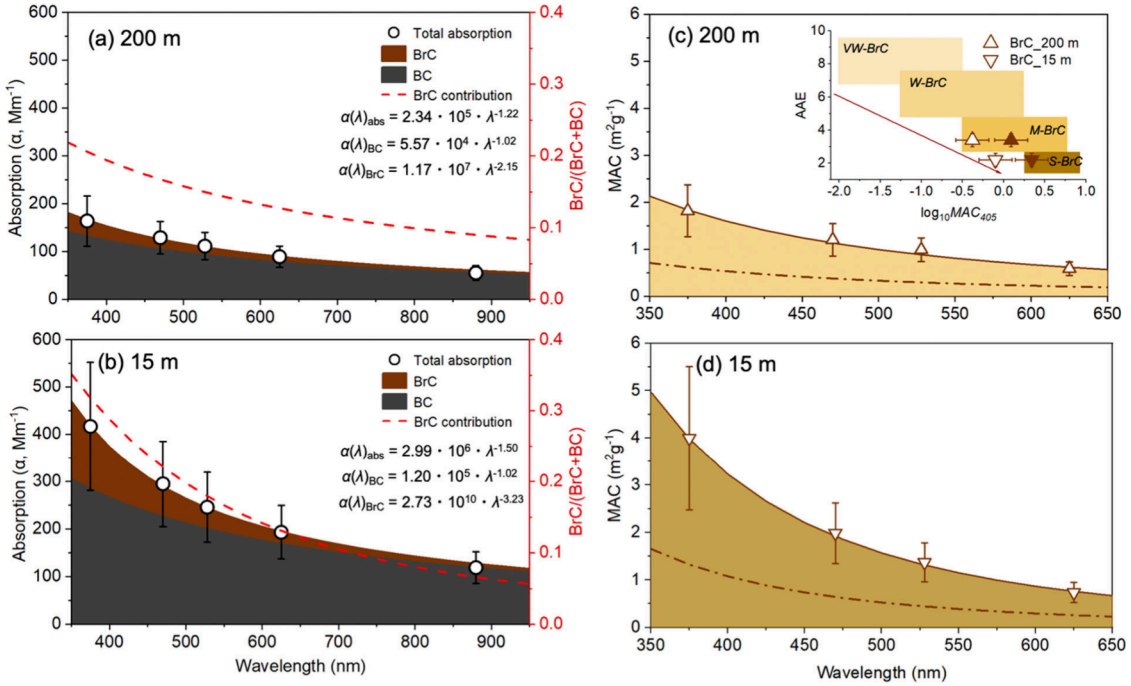

Figure 2. (a, b) Absorption coefficient measured by the UAV-mounted MA200 microaethalometer at 200 m (a) and 15 m (b) flight altitudes. Red dashed lines indicate the contribution of BrC to the total absorption. Error bars represent the standard errors over the full duration of each of the flights. (c, d) The mass absorption coefficient (MAC_λ) values ($m^2\ g^{-1}$) of BrC across a range of wavelengths at 200 m (c) and 15 m (d). Solid lines represent MAC values calculated using OPC-N3 mass concentrations; dashed lines represent SMPS-derived values. The inset in (c) shows classification of BrC reported at 200 and 15 m flight altitudes according to the optical framework proposed by Saleh.[39] The solid and open symbols represent MAC_{405nm} values estimated based on OPC-N3 SMPS-derived mass concentrations, respectively.

derived across a range of experimental temperatures (T) using[23] the Clausius–Clapeyron (eq 1) and ideal gas law eqs (eq 2).

$$ {}^{i}p_T^* = {}^{i}p_{T_{max}}^* \times \exp\left[\left(-\frac{{}^{i}\Delta H^*}{R}\right)\left(\frac{1}{T} - \frac{1}{T_{max}^*}\right)\right] \quad (1) $$

$$ {}^{i}C_T^* = \frac{{}^{i}p_T^* \times 10^9 \times {}^{i}\mathrm{MW}}{RT} \quad (2) $$

where T_{max}^* denotes the temperature at which peak ion intensity is observed in the extracted ion thermograms; ${}^{i}\Delta H^*$ is derived from the slope of the Arrhenius plots; ${}^{i}p_{T_{max}}^*$ is estimated based on the stoichiometry of the species' formal combustion oxidation reaction;[12] ^{i}MW is the molecular weight; and R is universal gas constant (8.3145 J mol^{-1} K^{-1}). The VBS framework, which categorizes organic compounds into discrete volatility bins,[6,24] is used to evaluate gas-particle partitioning behavior of OA. This analysis is based on species-specific values of ${}^{i}\Delta H^*$, ${}^{i}C_T^*$ and mass fractions, as detailed in our previous studies.[13,14] Viscosity (η, Pa·s) of individual components present in condensed-phase and their mixtures are estimated from their corresponding glass transition temperatures ($T_{g,i}$), predicted using elemental formulas and the Vogel–Fulcher–Tammann equation.[25,26] Corresponding diffusion coefficients (D_b) are calculated using the Stokes–Einstein equation,[27] enabling estimation of the characteristic mixing time scale (e-folding time (τ_{mix}), s).[28] Additionally, the viscosity of water-containing OA mixtures is calculated as a function of relative humidity (RH) using the Gordon–Taylor equation.[25,26] The explicit details of all calculations are provided in Supplemental Notes 2 and 3.

RESULTS AND DISCUSSION

Figure 1a shows the vertical profiles of mean particle number size distributions (PNSD) measured by the OPC-N3, revealing higher particle number concentrations at 15 m. The lowest OPC-N3 size channel includes particles >0.40 μm. At both altitudes, submicron particles dominated the number distributions, with concentrations decreasing toward larger sizes. Compared to the 15 m level, the 200 m profile exhibited significantly lower concentrations in both submicron (<1 μm) and supermicron (>1 μm) ranges, indicating a strong influence of primary emissions near the surface and aerosol dilution aloft. Notably, supermicron particles, with faster settling velocities, were predominantly observed at 15 m, consistent with biomass burning emissions from bonfires.[29] Figure 1b shows the calculated particle mass concentrations at 15 and 200 m, assuming a particle density of 1.59 g cm^{-3} reported in a previous campaign.[9] The mass concentrations of PM_1, $PM_{2.5}$, and PM_{10} were 8.1 ± 2.7 and 3.1 ± 2.5 $\mu g\ m^{-3}$, 15.1 ± 5.3 and 7.2 ± 6.3 $\mu g\ m^{-3}$, and 33.3 ± 18.6 and 18.6 ± 6.9 $\mu g\ m^{-3}$ at 15 and 200 m, respectively. The lower mass concentrations at 200 m align with prior observations of ambient OA levels measured aloft at similar altitudes.[30,31]

Figure 2 parts a and b present the wavelength-dependent absorption coefficients measured by MA200 at 15 and 200 m, revealing higher overall absorption at the low altitude. The average absorption Ångström exponent (AAE) values were 1.22 and 1.5 at 200 and 15 m. It is commonly assumed that light absorption by graphitic black carbon (BC) yields AAE values near 1, while standalone BrC typically exhibits AAE > 2.[1,32] However, various factors related to the mixing state of BC, BrC, and nonabsorbing components within individual ambient particles complicate the separation of their respective optical

https://doi.org/10.1021/acs.analchem.5c03027
Anal. Chem. 2025, 97, 17743−17751

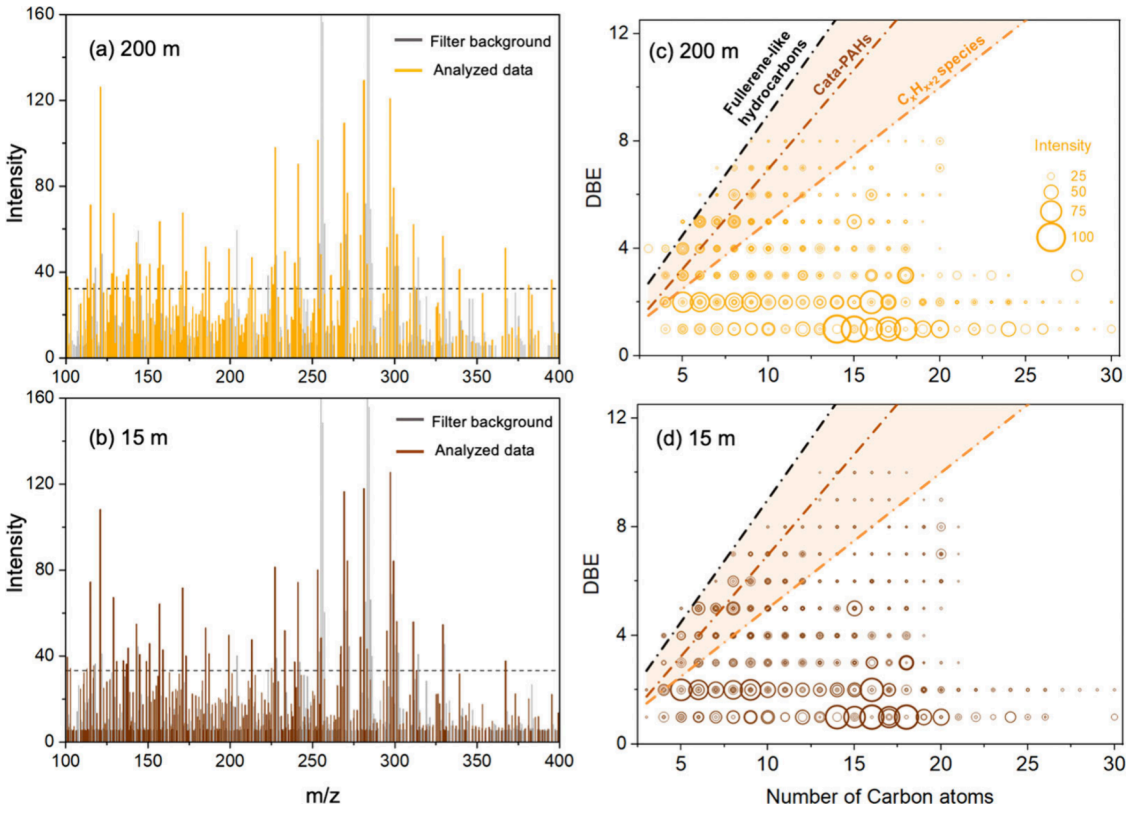

Figure 3. (a, b) Mass spectra obtained from TPD-DART-HRMS analysis of ambient OA collected at 200 m (a) and 15 m (b). Gray peaks represent background signals from blank filters, while orange (200 m) and brown (15 m) peaks indicate analyte signals. Peaks with intensities exceeding the dashed lines are those selected for TPD profile analysis. (c, d) Double bond equivalent (DBE) vs carbon number (C) plots for OA components detected at 200 m (c) and 15 m (d). References lines indicate DBE values of linear conjugated polyenes (orange line), cata-condensed PAHs (brown line), and fullerene-like hydrocarbons (black line). Data points within the orange shaded region indicate potential BrC chromophores.[45] Occasional data points above the fullerene-like line correspond to highly aromatic N-containing species. Marker size of the individual data points is proportional to the cube root of the corresponding mass spectral peaks intensities.

contributions.[33,34] Modeling studies have shown that AAE values in the range of 1−1.6 (consistent with our measured values of 1.22 and 1.5) are plausible for internally mixed BrC/BC particles.[35] The extent of these mixing-state effects is influenced by several particle-specific metrics, including the degree of internal and external mixing, the volume fractions and refractive indices of non-BC components, particle size and morphology, and core/shell structures.[33] Notably, ambient particles collected during Lag Ba'Omer events have been shown to possess substantial compositional and morphological complexity, as documented in our prior chemical imaging studies.[36,37] For the practical purposes of this study, the contribution of BrC to light absorption was estimated by subtracting the BC absorption component, assuming a characteristic AAE value of 1.02, following the procedure detailed in Supplemental Note 1.[9] At 375 nm, BrC accounted for 33% of total absorption at 15 m and 21% at 200 m, indicating a stronger BrC influence near the ground. This difference between the two heights decreases with increasing wavelength, and BrC absorption contributions converge at 600 nm. Notably, BrC contributions in this study exceed those reported for typical polluted urban environments, such as Beijing, Hong Kong, Seoul, and Osaka, where typical BrC contributions range from 12% to 14%,[38] likely due to the intense bonfires at the time of our study.

Figure 2 parts a and c show the calculated mass absorption coefficient (MAC_λ) values for BC and BrC components across a range of wavelengths. The BrC MAC_{375nm} values for ambient OA were 3.99 ± 1.51 $m^2\ g^{-1}$ at 15 m and 1.82 ± 0.71 $m^2\ g^{-1}$ at 200 m. Based on an established optical framework,[39] the aerosol is categorized as modestly absorbing BrC. MAC_λ values were derived from light absorption measurements by the MA200 and aerosol mass concentrations derived from OPC-N3 data, as detailed in Supplemental Note 1. However, OPC-N3 has been shown to underestimate $PM_{2.5}$ mass concentration.[40] For reference, ground-based measurements from a Scanning Mobility Particle Sizer (SMPS) on the same night of May 8, 2023, reported an average $PM_{2.5}$ mass concentration of 47.4 ± 2.6 $\mu g\ m^{-3}$, approximately three times higher than OPC-N3 estimates. Using these SMPS-derived values, the recalculated MAC_{375nm} for BrC is 1.29 ± 0.49 $m^2\ g^{-1}$ at 15 m and 0.59 ± 0.23 $m^2\ g^{-1}$ at 200 m, respectively. Additionally, potential overestimation of BrC absorption by the aethalometer may further inflate MAC values,[9] introducing some uncertainty into BrC classification. Despite these limitations, the data clearly indicate the influence of local bonfire emissions on BrC absorption near the ground.

While measuring light absorption, the microaethalometer collects aerosol samples, creating ∼3 mm spots on a PTFE filter tape, containing around 11−30 ng of particles as estimated by MA200 and OPC-N3 data, and ∼50−120 ng of particles following SMPS-based correction. TPD-DART-HRMS experiments require minimal sample mass and no additional sample preparation,[11,12] making it well-suited for analyzing chemical

https://doi.org/10.1021/acs.analchem.5c03027
Anal. Chem. 2025, 97, 17743−17751

composition of OA collected by the microaethalometer. In this study, TPD-DART-HRMS was employed to investigate the molecular composition and gas-particle partitioning of individual OA components. Figure 3 parts a and b show high-resolution mass spectra of OA samples collected at 200 and 15 m, respectively. Background peaks detected from the blank tape substrate were identified based on their characteristic m/z values and removed from the raw experimental data. Mass spectra of OA from both altitudes exhibit similar peaks in the m/z 100−350 range, indicating a well-mixed composition and a broad range of organic species present in the samples. Corresponding double bond equivalent (DBE) versus carbon number (C) plots (Figure 3c,d) reveal several abundant aliphatic compounds with low DBE values, differing from typical BBOA dominated by high-DBE aromatic species.[41,42] This deviation likely reflects the influence of various urban materials burned during the festival bonfires, including flammable construction waste, treated or painted wood, plywood, plastics, and other synthetic debris. Burning of these mixed urban materials produces complex emissions that differ from typical biomass burning, releasing not only highly aromatic BrC species but also elevated concentrations of aliphatic compounds. Figure S5 presents the composition of OA from controlled burns of select urban materials (carpet, manufactured wood, insulation, and vinyl tile), showing similar aliphatic compounds identified by TPD-DART-HRMS, which have also been shown in previous studies.[43,44] These findings suggest that burning of urban waste debris contributes significantly to the observed low-DBE aliphatic content in ambient OA reported here.

To quantify the volatility of OA components, 60 compounds with high peak abundances were selected for TPD profile analysis to derive values of ΔH^* and C^*_{298K}, following the data analysis approach from our previous studies.[13,14] This method provides formula-resolved apparent enthalpies ΔH^*. For example, for the species $C_{14}H_{28}O_2$, $C_{17}H_{34}O_4$, and $C_{19}H_{38}O_4$ in OA at 15-m, the derived ΔH^* values were 39.4 ± 0.3 kJ mol^{-1}, 53.7 ± 0.2 kJ mol^{-1}, and 66.9 ± 0.3 kJ mol^{-1}, respectively. The same compounds in OA at 200 m showed systematically higher ΔH^* values: 60.4 ± 0.3 kJ mol^{-1}, 63.8 ± 0.3 kJ mol^{-1}, and 96.3 ± 0.4 kJ mol^{-1}, as shown in Figure S5, respectively. The observed differences in ΔH^* among species with identical elemental composition likely reflect variations in Raoult's law matrix effects specific to each OA mixture, as well as plausible differences in isomeric composition.

Saturation gas-phase mass concentrations (C^*_T) across various temperatures were derived from the experimental ΔH^* and C^*_{298K} values (the full data set is provided in the Supporting Information file "VBS distribution"). Figure 4 shows the relationship between ΔH^* and log C^*_{298K} for all species, which aligns well with the previously reported fit lines for anthropogenic OA[46,47] and BBOA[48] based on thermodenuder studies. Similarly, findings from our recent studies on organic components of laboratory-generated BBOA proxies from wood pyrolysis emissions are also consistent with these observed trends.[14] In contrast, lab-generated biogenic SOA[13] and reference dicarboxylic acids[49] tend to follow the higher-volatility trend proposed by Epstein et al.,[50] which also served as the basis for a machine-learning model developed to predict the volatility of individual atmospherically relevant species.[51] However, ambient OA data consistently fall below this line, likely driven by matrix effects within the complex real-world OA mixtures. These results suggest that matrix effects, e.g., water content, presence of inorganic salts, in mixed OA systems can

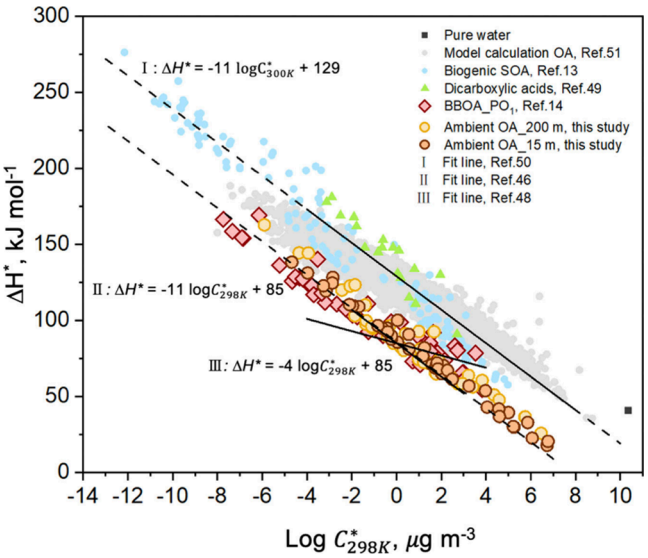

Figure 4. Relationship between apparent enthalpy of condensed-phase to gas-phase transition ($^i\Delta H^*$) and log C^*_{298K} for individual species in ambient OA mixtures derived from TPD-DART-HRMS measurements, compared with relevant reference data.[13,14,49,51] The fit lines I, II, and III correspond to biogenic SOA, anthropogenic OA, and BBOA, as proposed by Epstein et al.,[50] Ranjan et al.,[46] and May et al.,[48] respectively. Solid lines indicate the reported ranges of log C^*_{298K} values, while dashed lines represent extrapolations beyond those ranges.

significantly suppress component volatility. Additional factors - such as mixture viscosity, phase state, potential chemical transformations during storage, and interactions with the filter substrate - may also influence volatility and warrant further systematic investigation.

The C^*_T values derived from TPD-DART-HRMS measurements enable the construction of VBS distributions under varying atmospheric conditions of temperature T and total organic mass loadings (tOM), facilitating quantification of gas−particle partitioning of OA in ambient air.[13] Figure 5 parts a and b present the VBS distributions of OA components at 15 and 200 m under campaign conditions. The VBS distributions are similar between them, indicating a good degree of aerosol mixing within the urban boundary layer under 200 m. Temperature-dependent VBS distributions simulating atmospheric cooling are presented in Figure S6a−c. At 323 K, OA components primarily fall within the ranges of intermediate-volatility organic compounds[52] (IVOC, $10^2 < C^* \leq 10^6$, μg m^{-3}) and semivolatile organic compounds (SVOC, $10^{-2} < C^* \leq 10^2$, μg m^{-3}). As the temperature decreases to 273 K, the volatility of OA components shifts toward the SVOC and low volatility organic compounds (LVOC, $10^{-6} < C^* \leq 10^{-2}$, μg m^{-3}) ranges, increasing the particle-phase mass fraction from 49% to 80% as more compounds partition into the condensed phase. Similarly, the effect of dilution is shown in Figure S6d−f. At 298 K, the particle-phase mass fraction decreases from 75% at tOM = 100 μg m^{-3} to 41% at a tOM = 1 μg m^{-3}, primarily due to efficient gas-phase partitioning of IVOC and, to a lesser extent, partially SVOC species. LVOCs remain predominantly in the particle phase under all conditions. Comparison with VBS distributions from laboratory-generated BBOA,[14] ambient BBOA field data,[53,54] urban OA,[55] and modeled anthropogenic OA[56] (Figure S7) shows that the particle-phase distribution observed here resembles previous BBOA observations. However, unlike aerosol mass spectrometry (AMS), which probes solely

https://doi.org/10.1021/acs.analchem.5c03027
Anal. Chem. 2025, 97, 17743−17751

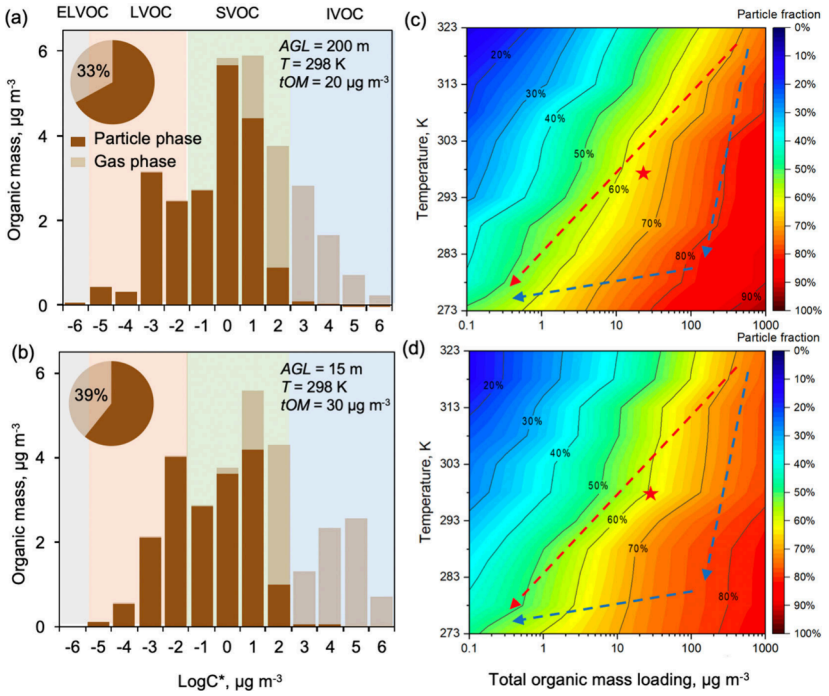

Figure 5. (a,b) VBS distributions constructed for OA mixtures at 200 m (a) and 15 m (b) under ambient conditions of *T* and *tOM*. Pie charts indicate the estimated mass fractions of total gas- and particle-phase species summed across all VBS bins. (c,d) Particle-phase mass fractions calculated at 200 m (c) and 15 m (d) based on the constructed VBS distributions over a range of ambient temperatures and total organic mass (*tOM*) loadings. Dashed lines represent rapid (blue) and gradual (red) cooling trajectories. Red stars indicate particle-phase mass fractions under the ambient conditions corresponding to each sampling height.

condensed-phase components, the TPD-DART-HRMS measurements also capture IVOCs, which mainly reside in the gas phase under ambient conditions, but tend to partition into the condensed phase when sampled air is pulled through the filter tape due to the filter adsorption artifacts.[57] This preconcentration effect enables the construction of more comprehensive VBS distributions that include IVOC species, which are typically underrepresented in AMS-based data sets. On the other hand, while 673 K (300 °C) is typically sufficient to vaporize SVOC and IVOC, less volatile components such as ELVOC, LVOC, and BC require higher temperatures for TPD-based detection,[58] where both evaporation and thermal decomposition begin to occur.[59] Our chemical imaging studies of individual particles collected during Lag Ba'Omer episodes indicate that the mass contribution of BC is comparable to that of the total organic fraction, based on particle-by-particle analysis.[36,37] This suggests that the VBS distributions constructed here likely underestimates the ELVOC and LVOC fractions. However, the impact of this underestimation is limited, as these low-volatility species do not participate significantly in gas-particle partitioning and remain predominantly in the particle phase under typical atmospheric conditions.

Two-dimensional (2D) maps were constructed to visualize the gas-particle partitioning of airborne OA mixtures at 15 and 200 m based on the corresponding VBS distributions, incorporating the combined effects of *T* and *tOM* conditions. This approach enables a comprehensive assessment of how atmospheric cooling, observed concentration, and dilution influence the partitioning behavior of organic constituents in aged OA plumes. Figure 5 parts c and d present these 2D maps for OA samples collected at 200 and 15 m, respectively, across a range of temperatures (273−323 K) and *tOM* loadings (0.1−1000 $\mu g\ m^{-3}$). Under these conditions, the particle-phase mass fractions vary from ∼20% to ∼90%. The gas-particle partitioning of OA mixtures during atmospheric transport is jointly influenced by cooling and dilution processes. In low-temperature environments, OA emissions rapidly cool, causing a rise and then decrease in particle fraction during atmospheric dilution, as shown by blue trajectories in Figure 5c,d. However, at warmer ambient temperatures, dilution effects may exceed cooling, resulting in slow progressive evaporation of species from the particle phase, shown by red trajectories in Figure 5c,d. These results indicate that atmospheric aging and vertical transport might influence the gas-particle partitioning of OA from ground emissions as it ascends through the atmosphere.

The transition of individual OA components from the particle to gas phases can be significantly constrained by diffusion limitations within particles. The apparent viscosity of OA mixtures can be estimated using mass-weighted viscosity values of all particle-phase species detected by TPD-DART-HRMS,[13] an approach previously validated by poke-flow experiments.[14] In particular, OA viscosity is influenced by the atmospheric factors such as *T* and *tOM* loading. Representative VBS distributions of OA color-coded by component-specific viscosity values, along with the viscosity maps corresponding to mixtures of the condensed-phase species as a function of *T* and *tOM*, are included in Figure S8. Most IVOC species exhibit viscosities below 10^4 Pa·s, facilitating rapid gas-particle partitioning. SVOC species span a broader viscosity range (10^4−10^{10} Pa·s), with their partitioning strongly affected by atmospheric conditions. LVOC and extremely low-volatility organic compounds (ELOVC) display very high viscosities (10^8−10^{12} Pa·s), indicating a glass-like solid state. Notably, when viscosity of the condensed-phase mixture exceeds 10^5 Pa·s, particle-to-gas partitioning becomes diffusion-limited, preserving OA species in the condensed phase.[14] Based on the viscosities of the remaining

https://doi.org/10.1021/acs.analchem.5c03027
Anal. Chem. 2025, 97, 17743−17751

species in the particle phase and their corresponding mass contribution, Figure 6 presents the estimated viscosities of OA

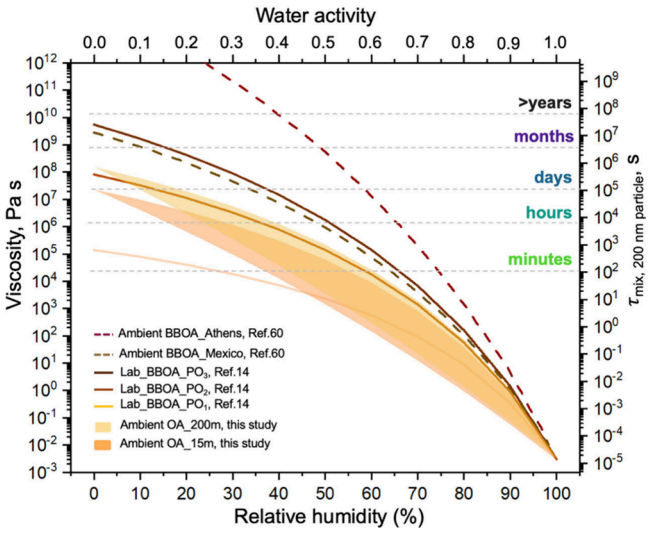

Figure 6. Estimated viscosity and characteristic mixing times of ambient OA as a function of relative humidity (RH), shown in comparison with previously reported values.[14,60]

mixtures as a function of RH. Under dry conditions, the calculated viscosity values are $10^{7.3}$ Pa·s and $10^{8.1}$ Pa·s at 15 and 200 m, respectively, indicating that OA particles might be slightly more viscous at higher altitudes. This plausible increase in viscosity is consistent with evaporative aging during the upward transport of OA, driven by gas-phase partitioning of IVOC and SVOC components and the concurrent enrichment of LVOC and ELVOC species in the particle phase due to dilution and cooling at higher altitudes.[14] Additionally, atmospheric oxidation likely enhances viscosity further by producing more oxidized, higher-molecular-weight compounds that partition into the condensed phase. High viscosity reduces particle-phase diffusion rates and significantly prolongs equilibration times. As shown in Figure 6, the characteristic *e*-folding mixing times for dry OA mixtures discussed in this study are on the order of hours to days. These results suggest that locally emitted OA may transition into amorphous solid glass-like particles under low RH, with atmospheric reactivity largely limited to their surface processes.

The viscosity and diffusion of ambient OA are strongly influenced by its water activity.[61−63] Figure 6 illustrates RH-dependent estimates of OA viscosity and diffusion at 15 and 200 m, calculated under equilibrium hygroscopicity conditions using an effective hygroscopicity parameter $\kappa = 0.057 \pm 0.07$ reported for BBOA particles.[64] Viscosity decreases significantly with increasing RH, particularly above 50%, leading to a rapid reduction in *e*-folding mixing times to less than one second. Additionally, Figure 6 compares the viscosity estimates of OA mixtures at both heights with those of ambient BBOA,[60] lab-generated BBOA,[14] and biogenic SOA.[13] Viscosity of OA estimated in our study closely resembles that of laboratory BBOA subjected to evaporation, with volume reduction factors of ~2 (annotated as PO_2). These values are also consistent with ambient OA influenced by biomass burning in Mexico City, but are lower than those reported in Athens under similar influence, likely reflecting differences in local sources and atmospheric conditions.[60] Overall, the presented viscosity calculations highlight the value of integrating the viscosity and diffusion estimation approach presented here with aethalometer observations in future studies.

CONCLUSIONS AND ATMOSPHERIC SIGNIFICANCE

Our study presents the first application of TPD-DART-HRMS in conjunction with aethalometer measurements, enabling a comparative investigation of OA light-absorbing properties alongside detailed chemical characterization. Traditionally used to measure light absorption by carbonaceous aerosols, the microaethalometer deployed on a mobile UAV platform was complemented with high-resolution temperature-programmed desorption and molecular analysis of collected samples to characterize OA composition and volatility. This integration enables quantitative assessments of gas−particle partitioning and viscosity in samples of ambient OA, directly correlated with its BrC optical properties. This combined approach offers a powerful and practical method to link optical and chemical properties of OA, using low-mass samples collected on the aethalometer's filter tape.

Our findings demonstrate that the gas-particle partitioning of OA is strongly influenced by atmospheric *T* and *tOM*, key factors that should be accounted for in atmospheric simulations of OA dynamics. We show that although the aerosol mixing below 200 m within the urban boundary layer is relatively efficient, OA viscosity may increase with altitude, driven by evaporative aging and compositional changes during vertical transport. The increased viscosity may promote particle solidification, extend atmospheric lifetime, and influence OA impacts on radiative forcing and aerosol-cloud interactions.

Various multiphase reactions can darken BrC aerosols within hours of emission, while photobleaching and oxidative whitening may occur after a day or more.[65,66] Heat generated by biomass burning can enhance vertical transport through convection, facilitating the uplift of BrC into the mid- and upper troposphere, especially during nighttime, when the planetary boundary layer is shallow (~200−300 m).[67−69] Moreover, the pronounced decoupling of gas-to-particle conversion was observed at varying altitudes, resulting in distinct physicochemical features and atmospheric processes.[70] Therefore, investigating the effects of vertical transport on the chemical composition and physical properties of OA aerosols and their BrC components are essential for understanding their role in atmospheric chemistry and climate,[5,39] This is particularly critical as emissions from biomass burning continue to increase globally.[71,72]

The new methodology for comprehensively characterizing ambient OA highlights the potential for future systematic investigations that integrate light absorption with detailed chemical composition, offering deeper insight into BrC's role in the atmospheric environment. It provides a new experimental framework for studying the properties and evolution of BBOA emissions across a range of spatial and temporal contexts. Moreover, this approach is broadly applicable to study OA from different emission sources, enabling integrated analysis of aerosol composition, volatility, and optical properties under varying atmospheric environments.

ASSOCIATED CONTENT

Supporting Information

The Supporting Information is available free of charge at https://pubs.acs.org/doi/10.1021/acs.analchem.5c03027.

https://doi.org/10.1021/acs.analchem.5c03027
Anal. Chem. 2025, 97, 17743−17751

Supplemental Notes S1−S6: Field deployment and real-time measurements; construction of VBS distributions; viscosity, diffusion coefficient, and *e*-folding time calculations; molecular composition of OA from burning urban materials; VBS distributions and gas-particle partitioning of OA mixtures under variable *T* and *tOM* conditions; viscosity of OA mixtures as a function of RH and *T*. Figures S1−S8 and Table S1, illustrating the supplemental notes (PDF)

VBS distribution−template (XLSX)

AUTHOR INFORMATION

Corresponding Author

Alexander Laskin − *Department of Chemistry and Department of Earth, Atmospheric, and Planetary Sciences, Purdue University, West Lafayette, Indiana 47907, United States;* orcid.org/0000-0002-7836-8417; Email: alaskin@purdue.edu

Authors

Qiaorong Xie − *Department of Chemistry, Purdue University, West Lafayette, Indiana 47907, United States;* orcid.org/0000-0002-9391-624X

Eli Windwer − *Department of Earth and Planetary Sciences, Weizmann Institute of Science, Rehovot 76100, Israel*

Isaac S. Morton − *Davidson School of Chemical Engineering, Purdue University, West Lafayette, Indiana 47907, United States*

Kelsey E. Lavin − *Department of Chemistry, Purdue University, West Lafayette, Indiana 47907, United States*

Emily R. Halpern − *Department of Chemistry, Purdue University, West Lafayette, Indiana 47907, United States;* orcid.org/0000-0003-2009-6807

Dori Nissenbaum − *Department of Earth and Planetary Sciences, Weizmann Institute of Science, Rehovot 76100, Israel*

Sergey A. Nizkorodov − *Department of Chemistry, University of California, Irvine, Irvine, California 92697, United States;* orcid.org/0000-0003-0891-0052

Yinon Rudich − *Department of Earth and Planetary Sciences, Weizmann Institute of Science, Rehovot 76100, Israel;* orcid.org/0000-0003-3149-0201

Complete contact information is available at: https://pubs.acs.org/10.1021/acs.analchem.5c03027

Notes

The authors declare no competing financial interest.

ACKNOWLEDGMENTS

The field campaign of this research was supported by the international collaboration grant from the US National Science Foundation (NSF Grant AGS-2039985) and the US-Israel Binational Science Foundation (BSF Grant 2020656). The laboratory experiments were supported by the National Oceanic and Atmospheric Administration grants NA22OAR4310195 (Purdue University) and NA22OAR4310196 (University of California, Irvine). ERH acknowledges support from the Bilsland Dissertation Fellowship provided by the Department of Chemistry and the Graduate School of Purdue University.

REFERENCES

(1) Laskin, A.; Laskin, J.; Nizkorodov, S. A. *Chem. Rev.* **2015**, *115* (10), 4335.

(2) Andreae, M. O.; Gelencsér, A. *Atmos. Chem. Phys.* **2006**, *6* (10), 3131−3148.

(3) Xiong, R.; Li, J.; Zhang, Y.; Zhang, L.; Jiang, K.; Zheng, H.; Kong, S.; Shen, H.; Cheng, H.; Shen, G. *Environ. Sci. Ecotechnol.* **2022**, *12*, No. 100201.

(4) Chung, C. E.; Ramanathan, V.; Decremer, D. *Proc. Natl. Acad. Sci. U.S.A.* **2012**, *109* (29), 11624−11629.

(5) Brown, H.; Liu, X.; Pokhrel, R.; Murphy, S.; Lu, Z.; Saleh, R.; Mielonen, T.; Kokkola, H.; Bergman, T.; Myhre, G.; Skeie, R. B.; Watson-Paris, D.; Stier, P.; Johnson, B.; Bellouin, N.; Schulz, M.; Vakkari, V.; Beukes, J. P.; van Zyl, P. G.; Liu, S.; Chand, D. *Nat. Commun.* **2021**, *12* (1), 277.

(6) Donahue, N. M.; Kroll, J.; Pandis, S. N.; Robinson, A. L. *Atmos. Chem. Phys.* **2012**, *12* (2), 615−634.

(7) Isaacman-VanWertz, G.; Massoli, P.; O'Brien, R.; Lim, C.; Franklin, J. P.; Moss, J. A.; Hunter, J. F.; Nowak, J. B.; Canagaratna, M. R.; Misztal, P. K.; Arata, C.; Roscioli, J. R.; Herndon, S. T.; Onasch, T. B.; Lambe, A. T.; Jayne, J. T.; Su, L.; Knopf, D. A.; Goldstein, A. H.; Worsnop, D. R.; Kroll, J. H. *Nat. Chem.* **2018**, *10* (4), 462−468.

(8) Wang, Q.; Wang, L.; Gong, C.; Li, M.; Xin, J.; Tang, G.; Sun, Y.; Gao, J.; Wang, Y.; Wu, S.; Kang, Y.; Yang, Y.; Li, T.; Liu, J.; Wang, Y. *Sci. Total Environ.* **2022**, *806*, No. 150950.

(9) Li, C.; Windwer, E.; Fang, Z.; Nissenbaum, D.; Rudich, Y. *Sci. Total Environ.* **2021**, *777*, No. 146143.

(10) Zhang, X.; Xu, J.; Kang, S.; Sun, J.; Shi, J.; Gong, C.; Sun, X.; Du, H.; Ge, X.; Zhang, Q. *J. Geophys. Res.-Atmos.* **2021**, *126* (24), No. e2021JD035562.

(11) Xie, Q.; Laskin, A. *TrAC-Trend Anal. Chem.* **2024**, *181*, No. 117986.

(12) West, C. P.; Hsu, Y.-J.; MacFeely, K. T.; Huston, S. M.; Aridjis-Olivos, B. P.; Morales, A. C.; Laskin, A. *Anal. Chem.* **2023**, *95* (19), 7403−7408.

(13) Xie, Q.; Halpern, E. R.; Zhang, J.; Shrivastava, M.; Zelenyuk, A.; Zaveri, R. A.; Laskin, A. *Anal. Chem.* **2024**, *96* (23), 9524−9534.

(14) Xie, Q.; Gerrebos, N. G. A.; Calderon-Arrieta, D.; Morton, I. S.; Halpern, E. R.; Li, C.; Zeng, M. F.; Bertram, A. K.; Rudich, Y.; Laskin, A. *Environ. Sci. Technol.* **2024**, *58* (41), 18284−18294.

(15) Siemens, K.; Paik, T.; Li, A.; Rivera-Adorno, F.; Tomlin, J.; Xie, Q.; Chakrabarty, R. K.; Laskin, A. *ACS Earth Space Chem.* **2024**, *8* (7), 1416−1428.

(16) Alas, H. D. C.; Müller, T.; Weinhold, K.; Pfeifer, S.; Glojek, K.; Gregorič, A.; Močnik, G.; Drinovec, L.; Costabile, F.; Ristorini, M.; Wiedensohler, A. *Aerosol Air Qual Res.* **2020**, *20* (12), 2640−2653.

(17) Crilley, L. R.; Shaw, M.; Pound, R.; Kramer, L. J.; Price, R.; Young, S.; Lewis, A. C.; Pope, F. D. *Atmos. Meas. Technol.* **2018**, *11* (2), 709−720.

(18) Bezantakos, S.; Schmidt-Ott, F.; Biskos, G. *Aerosol Sci. Technol.* **2018**, *52* (4), 385−392.

(19) Bluvshtein, N.; Lin, P.; Flores, J. M.; Segev, L.; Mazar, Y.; Tas, E.; Snider, G.; Weagle, C.; Brown, S. S.; Laskin, A.; Rudich, Y. *J. Geophys. Res.-Atmos.* **2017**, *122* (10), 5441−5456.

(20) Adler, G.; Flores, J.; Abo Riziq, A.; Borrmann, S.; Rudich, Y. *Atmos. Chem. Phys.* **2011**, *11* (4), 1491−1503.

(21) Lin, P.; Bluvshtein, N.; Rudich, Y.; Nizkorodov, S. A.; Laskin, J.; Laskin, A. *Environ. Sci. Technol.* **2017**, *51* (20), 11561−11570.

(22) Roach, P. J.; Laskin, J.; Laskin, A. *Anal. Chem.* **2011**, *83* (12), 4924−4929.

(23) Chattopadhyay, S.; Tobias, H. J.; Ziemann, P. J. *Anal. Chem.* **2001**, *73* (16), 3797−3803.

(24) Donahue, N. M.; Epstein, S. A.; Pandis, S. N.; Robinson, A. L. *Atmos. Chem. Phys.* **2011**, *11* (7), 3303−3318.

(25) DeRieux, W.-S. W.; Li, Y.; Lin, P.; Laskin, J.; Laskin, A.; Bertram, A. K.; Nizkorodov, S. A.; Shiraiwa, M. *Atmos. Chem. Phys.* **2018**, *18* (9), 6331−6351.

(26) Galeazzo, T.; Valorso, R.; Li, Y.; Camredon, M.; Aumont, B.; Shiraiwa, M. *Atmos. Chem. Phys.* **2021**, *21* (13), 10199−10213.

(27) Koop, T.; Bookhold, J.; Shiraiwa, M.; Pöschl, U. *Phys. Chem. Chem. Phys.* **2011**, *13* (43), 19238−19255.

(28) Shiraiwa, M.; Ammann, M.; Koop, T.; Pöschl, U. *Proc. Natl. Acad. Sci. U.S.A.* **2011**, *108* (27), 11003−11008.
(29) Reicher, N.; Budke, C.; Eickhoff, L.; Raveh-Rubin, S.; Kaplan-Ashiri, I.; Koop, T.; Rudich, Y. *Atmos. Chem. Phys.* **2019**, *19* (17), 11143−11158.
(30) Zhou, W.; Sun, Y.; Xu, W.; Zhao, X.; Wang, Q.; Tang, G.; Zhou, L.; Chen, C.; Du, W.; Zhao, J.; Xie, C.; Fu, P.; Wang, Z. *J. Geophys. Res.-Atmos.* **2018**, *123* (22), 13.016−13.029.
(31) Qiu, Y.; Xie, Q.; Wang, J.; Xu, W.; Li, L.; Wang, Q.; Zhao, J.; Chen, Y.; Chen, Y.; Wu, Y.; Du, W.; Zhou, W.; Lee, J.; Zhao, C.; Ge, X.; Fu, P.; Wang, Z.; Worsnop, D. R.; Sun, Y. *ACS Earth Space Chem.* **2019**, *3* (2), 273−284.
(32) Laskin, A.; West, C. P.; Hettiyadura, A. P. *Chem. Soc. Rev.* **2025**, *54*, 1583.
(33) Kong, Y.; Zhi, G.; Jin, W.; Zhang, Y.; Shen, Y.; Li, Z.; Sun, J.; Ren, Y. *Sci. Total Environ.* **2024**, *924*, No. 171539.
(34) Li, W.; Riemer, N.; Xu, L.; Wang, Y.; Adachi, K.; Shi, Z.; Zhang, D.; Zheng, Z.; Laskin, A. *npj Clim. Atmos. Sci.* **2024**, *7* (1), 65.
(35) Lack, D.; Cappa, C. *Atmos. Chem. Phys.* **2010**, *10* (9), 4207−4220.
(36) Tomlin, J. M.; Weis, J.; Veghte, D. P.; China, S.; Fraund, M.; He, Q.; Reicher, N.; Li, C.; Jankowski, K. A.; Rivera-Adorno, F. A.; Morales, A. C.; Rudich, Y.; Moffet, R. C.; Gilles, M. K.; Laskin, A. *Environ. Sci. Atmos.* **2022**, *2* (4), 616−633.
(37) Rivera-Adorno, F. A.; Sharpe, S. A. L.; Olayemi, T. E.; Ese, J. I.; Fraund, M.; Moffet, R. C.; TC, A.; Windwer, E.; Fang, Z.; Valencia-Acuna, P.; O'Callahan, B. T.; El-Khoury, P.; Rudich, Y.; Laskin, A. *Aerosol Sci. Technol.* **2025**, 1−17.
(38) Cho, C.; Kim, S.-W.; Lee, M.; Lim, S.; Fang, W.; Gustafsson, Ö.; Andersson, A.; Park, R. J.; Sheridan, P. J. *Atmos. Environ.* **2019**, *212*, 65−74.
(39) Saleh, R. *Current Pollution Reports* **2020**, *6*, 90−104.
(40) Kaur, K.; Kelly, K. E. *Atmos. Meas. Technol.* **2023**, *16* (10), 2455−2470.
(41) Xu, C.; Gao, L.; Lyu, Y.; Qiao, L.; Huang, D.; Liu, Y.; Li, D.; Zheng, M. *Environ. Int.* **2022**, *167*, No. 107421.
(42) Lin, P.; Aiona, P. K.; Li, Y.; Shiraiwa, M.; Laskin, J.; Nizkorodov, S. A.; Laskin, A. *Environ. Sci. Technol.* **2016**, *50* (21), 11815−11824.
(43) Hopstock, K. S.; Klodt, A. L.; Xie, Q.; Alvarado, M. A.; Laskin, A.; Nizkorodov, S. A. *Environ. Sci. Atmos.* **2023**, *3* (9), 1272−1285.
(44) Hopstock, K. S.; Xie, Q.; Alvarado, M. A.; Moschos, V.; Bililign, S.; Surratt, J. D.; Laskin, A.; Nizkorodov, S. A. *ACS ES&T Air* **2024**, *1* (11), 1495−1506.
(45) Lin, P.; Fleming, L. T.; Nizkorodov, S. A.; Laskin, J.; Laskin, A. *Anal. Chem.* **2018**, *90* (21), 12493−12502.
(46) Ranjan, M.; Presto, A. A.; May, A. A.; Robinson, A. L. *Aerosol Sci. Technol.* **2012**, *46* (1), 13−21.
(47) May, A. A.; Presto, A. A.; Hennigan, C. J.; Nguyen, N. T.; Gordon, T. D.; Robinson, A. L. *Environ. Sci. Technol.* **2013**, *47* (15), 8288−8296.
(48) May, A. A.; Levin, E. J.; Hennigan, C. J.; Riipinen, I.; Lee, T.; Collett, J. L., Jr; Jimenez, J. L.; Kreidenweis, S. M.; Robinson, A. L. *J. Geophys. Res.-Atmos.* **2013**, *118* (19), 11.327−11.338.
(49) Bilde, M.; Barsanti, K.; Booth, M.; Cappa, C. D.; Donahue, N. M.; Emanuelsson, E. U.; McFiggans, G.; Krieger, U. K.; Marcolli, C.; Topping, D.; et al. *Chem. Rev.* **2015**, *115* (10), 4115−4156.
(50) Epstein, S. A.; Riipinen, I.; Donahue, N. M. *Environ. Sci. Technol.* **2010**, *44* (2), 743−748.
(51) Besel, V.; Todorović, M.; Kurtén, T.; Rinke, P.; Vehkamäki, H. *Sci. Data* **2023**, *10* (1), 450.
(52) Donahue, N. M.; Robinson, A. L.; Trump, E. R.; Riipinen, I.; Kroll, J. H. *Atmos. Aerosol Chem.* **2012**, *339*, 97−143.
(53) Feng, T.; Wang, Y.; Hu, W.; Zhu, M.; Song, W.; Chen, W.; Sang, Y.; Fang, Z.; Deng, W.; Fang, H.; Yu, X.; Wu, C.; Yuan, B.; Huang, S.; Shao, M.; Huang, X.; He, L.; Lee, Y. R.; Huey, L. G.; Canonaco, F.; Prevot, A. S. H.; Wang, X. *Atmos. Chem. Phys.* **2023**, *23* (1), 611−636.
(54) Xu, W.; Chen, C.; Qiu, Y.; Li, Y.; Zhang, Z.; Karnezi, E.; Pandis, S. N.; Xie, C.; Li, Z.; Sun, J.; Ma, N.; Xu, W.; Fu, P.; Wang, Z.; Zhu, J.; Worsnop, D. R.; Ng, N. L.; Sun, Y. *Atmos. Chem. Phys.* **2021**, *21* (7), 5463−5476.
(55) Zhang, Y.; Huang, H.; Qin, W.; Yu, Q.; Sun, Y.; Cheng, S.; Ahmad, M.; Ouyang, W.; Soyol-Erdene, T.-O.; Chen, J. *Carbon Res.* **2023**, *2* (1), 6.
(56) Voliotis, A.; Wang, Y.; Shao, Y.; Du, M.; Bannan, T. J.; Percival, C. J.; Pandis, S. N.; Alfarra, M. R.; McFiggans, G. *Atmos. Chem. Phys.* **2021**, *21* (18), 14251−14273.
(57) Turpin, B. J.; Huntzicker, J. J.; Hering, S. V. *Atmos. Environ.* **1994**, *28* (19), 3061−3071.
(58) Tasoglou, A.; Louvaris, E.; Florou, K.; Liangou, A.; Karnezi, E.; Kaltsonoudis, C.; Wang, N.; Pandis, S. N. *Atmos. Chem. Phys.* **2020**, *20* (19), 11625−11637.
(59) Halpern, E.; Heirty, L.; West, C.; Li, Y.; Kim, W. M.; Mennito, A. S.; Laskin, A. *Environmental Science: Processes & Impacts* **2025**, *27* (1), 104−118.
(60) Li, Y.; Day, D. A.; Stark, H.; Jimenez, J. L.; Shiraiwa, M. *Atmos. Chem. Phys.* **2020**, *20* (13), 8103−8122.
(61) Schnitzler, E. G.; Gerrebos, N. G.; Carter, T. S.; Huang, Y.; Heald, C. L.; Bertram, A. K.; Abbatt, J. P. *Proc. Natl. Acad. Sci. U.S.A.* **2022**, *119* (38), No. e2205610119.
(62) Gregson, F. K.; Gerrebos, N. G.; Schervish, M.; Nikkho, S.; Schnitzler, E. G.; Schwartz, C.; Carlsten, C.; Abbatt, J. P.; Kamal, S.; Shiraiwa, M.; Bertram, A. K. *Environ. Sci. Technol.* **2023**, *57* (39), 14548−14557.
(63) Evoy, E.; Kiland, K. J.; Huang, Y.; Schnitzler, E. G.; Maclean, A. M.; Kamal, S.; Abbatt, J. P.; Bertram, A. K. *ACS Earth Space Chem.* **2021**, *5* (11), 3268−3278.
(64) Bougiatioti, A.; Bezantakos, S.; Stavroulas, I.; Kalivitis, N.; Kokkalis, P.; Biskos, G.; Mihalopoulos, N.; Papayannis, A.; Nenes, A. *Atmos. Chem. Phys.* **2016**, *16* (11), 7389−7409.
(65) Hems, R. F.; Schnitzler, E. G.; Liu-Kang, C.; Cappa, C. D.; Abbatt, J. P. *ACS Earth Space Chem.* **2021**, *5* (4), 722−748.
(66) Sedlacek III, A. J.; Lewis, E. R.; Onasch, T. B.; Zuidema, P.; Redemann, J.; Jaffe, D.; Kleinman, L. I. *Environ. Sci. Technol.* **2022**, *56* (20), 14315−14325.
(67) Zhang, Y.; Forrister, H.; Liu, J.; Dibb, J.; Anderson, B.; Schwarz, J. P.; Perring, A. E.; Jimenez, J. L.; Campuzano-Jost, P.; Wang, Y.; Nenes, A.; Weber, R. J. *Nat. Geosci.* **2017**, *10* (7), 486−489.
(68) Jin, X.; Cai, X.; Yu, M.; Wang, X.; Song, Y.; Kang, L.; Zhang, H.; Zhu, T. *Atmos. Environ.* **2021**, *258*, No. 118511.
(69) Quan, J.; Gao, Y.; Zhang, Q.; Tie, X.; Cao, J.; Han, S.; Meng, J.; Chen, P.; Zhao, D. *Particuology* **2013**, *11* (1), 34−40.
(70) Du, W.; Dada, L.; Zhao, J.; Chen, X.; Daellenbach, K. R.; Xie, C.; Wang, W.; He, Y.; Cai, J.; Yao, L.; Zhang, Y.; Wang, Q.; Xu, W.; Wang, Y.; Tang, G.; Cheng, X.; Kokkonen, T. V.; Zhou, W.; Yan, C.; Chu, B.; Zha, Q.; Hakala, S.; Kurppa, M.; Jarvi, L.; Liu, Y.; Li, Z.; Ge, M.; Fu, P.; Nie, W.; Bianchi, F.; Petaja, T.; Paasonen, P.; Wang, Z.; Worsnop, D. R.; Kerminen, V.-M.; Kulmala, M.; Sun, Y. *npj Clim. Atmos. Sci.* **2021**, *4* (1), 4.
(71) Palm, B. B.; Peng, Q.; Fredrickson, C. D.; Lee, B. H.; Garofalo, L. A.; Pothier, M. A.; Kreidenweis, S. M.; Farmer, D. K.; Pokhrel, R. P.; Shen, Y.; Murphy, S. M.; Permar, W.; Hu, L.; Campos, T. L.; Hall, S. R.; Ullmann, K.; Zhang, X.; Flocke, F.; Fischer, E. V.; Thornton, J. A. *Proc. Natl. Acad. Sci. U.S.A.* **2020**, *117* (47), 29469−29477.
(72) Farley, R.; Bernays, N.; Jaffe, D. A.; Ketcherside, D.; Hu, L.; Zhou, S.; Collier, S.; Zhang, Q. *Environ. Sci. Technol.* **2022**, *56* (6), 3645−3657.

https://doi.org/10.1021/acs.analchem.5c03027
Anal. Chem. 2025, 97, 17743−17751